Chen, R., et al., 2023, Martian soil as revealed by ground-penetrating radar at the Tianwen-1 landing site: Geology, https://doi.org/10.1130/G50632.1

Supplementary Materials for

Martian soil as revealed by the ground-penetrating-radar at the Tianwen-1 landing site

Ruonan Chen[1,†], Ling Zhang[1,2,†], Yi Xu[1,*], Renrui Liu[1], Roberto Bugiolacchi[1,3], Xiaoping Zhang[1], Lu Chen[1], Zhaofa Zeng[2] , Cai Liu[2]

1. State Key Laboratory of Lunar and Planetary Sciences, Macau University of Science and Technology, Macau, China.

2. College of Geo-exploration Science and Technology, Jilin University, Changchun 130026, China.

3. Earth Sciences, University College London, London, UK.

[*]*Corresponding author. Email: yixu@must.edu.mo*

[†]*Two authors contribute equally.*

This Supplementary Information includes:

Supplementary Text

Figs. S1 to S14

Table. S1 to S2

Supplementary References

Supplementary Text

1. Remote Sensing Observations of Martian Soil.

Telescope imaging and a succession of orbiter and terrain cameras have provided imagery of the surface (e.g., Kirk et al. 2008), such as the High-Resolution Imaging Science Experiment (HiRISE, 0.25 m/pixel) aboard the MRO science mission. The global thermal inertia map based on data from the Thermal Emission Spectrometer (TES) instrument has shown that the thermal inertia varies significantly. Different thermal inertia values may be caused by differences in bulk porosity, grain size, as well as the state of cementation or induration. Although the bulk composition of the martian soil is like Earth's basalts (e.g., Bandfield et al. 2003), they also show regional variances. The TES identified two global-scale volcanic units on Mars: one characterizes the Noachian-aged highlands and consists of unaltered plagioclase- and clinopyroxene-rich basalts; the other is found in the younger plains north of the dichotomy boundary and is richer in silica (e.g., Christensen et al. 2008). Similar conclusions were reached based on data garnered by the Mini-TES on the Spirit rover within the Gusev Crater and the Opportunity rover in the Eagle Crater (e.g., McSween et al. 2010; Rogers et al. 2008). However, the materials detected by the CheMin instrument

on the Curiosity rover in the Gale Crater are slightly different, which also include heterogeneous species rich in Fe^{3+} and volatiles (e.g., Blake et al. 2013).

Martian dust is similar in composition to the global soil unit and bulk basaltic Mars crust, as assessed by the Alpha-Particle X-ray Spectrometer (APXS) measurements, but also enriched in S and Cl (e.g., Berger et al. 2016). These findings are also congruent with the martian dust and soil compositions based on data from the Mars rover missions (e.g., Goetz et al. 2005). However, the thickness of the global dust layer is non-uniform, ranging from zero to tens of meters (e.g., Ruff et al. 2006). An alternative and more direct measurement than thermal inertia or albedo is the global dust cover index (DCI), which clearly shows differences in thickness (e.g., Ruff et al. 2002). The DCI in TES spectra suggest that the dust-covered areas are prevalent in the north, while the south features more dust-free areas.

2. Geological Settings

Diverse types of geomorphological features characterize the region of the Zhurong landing site, including polygonal troughs, linear or curvilinear ridges, pitted cones, mesas, dunes and various crater ejecta deposits (e.g., Zhao et al. 2022). Both the TES albedo (0.234) and the DCI (0.941±0.011) indicate that the surface of the study area is relatively dusty at the TES spatial resolution (~3 km by ~5 km). The permittivity of surface materials in the Utopia Planitia is ~3-4, as derived from SHARAD (e.g., Castaldo et al. 2017), and ~4-5 from MARSIS data (e.g., Mouginot et al. 2012). This disparity is due to different radar wavelengths being employed and corresponding detection depths.

The Zhurong rover, released by the lander, traversed about 1.2 km southward in the first six months, navigating around dunes and driving on small craters or small rocks where possible, as illustrated in Fig. 1A, on terrains with a gradually decreasing surface elevation (Fig. 4). Geomorphologically and topographically, the surface terrain during this traverse remains flat and smooth with an average slope of 3±0.2° in most areas, facilitating long-distance traversal. Tens of impact craters with a diameter of 2-10 m with varying degrees of degradation can be seen in orbital images along this traverse, such as those indicated by cyan arrows in Fig. 1A. Some show relatively high albedo and protuberant rims, and others have little relief, which makes it difficult to assess whether they are either primary or secondary impacts. Many rocks of various sizes (smaller than 2 m) are scattered on and around the exploration path. Over two million rocks with diameters ranging from 1.4 to 8 m were also observed from the high-resolution imaging camera (HiRIC; 0.7 m/pixel) mosaics within the landing region. Some of the rocks seen by NaTeCam are clearly fluted, suggesting aeolian abrasion. Aeolian bedforms are also commonly found along the exploration path.

3. Data and Instruments.

Mars Reconnaissance Orbiter (MRO) High-Resolution Imaging Science Experiment (HiRISE; 0.25 m/pixel) data[1] were used to characterize geomorphological features of the Zhurong landing area.

Zhurong is equipped with six scientific instruments (e.g. Tan et al. 2021), including (a) the Mars Surface Composition Detector (MarSCoDe) using a Laser Induced Breakdown Spectrometer and a Visible and Near Infrared Spectrometer (VNIS: 850–2400 nm) mineralogy detector; (b) a Multispectral Camera (MSCam: 470–1025 nm); the Mars Rover

Penetrating Radar (RoPeR) with dual-frequency channels (CH1: 35-75 MHz; CH2:0.45-2.15 GHz); (d) the Mars Rover Magnetometer (RoMAG); (e) Mars Climate Station (MCS); and the Navigation and Terrain Camera (NaTeCam).

The Navigation and Terrain Cameras (NaTeCams) mounted on the Zhurong rover are binocular stereo cameras, which are primarily designed to provide support for the guidance, navigation, and control of the rover. They are used for three-dimensional panoramic imaging of the surface and for studying topographical and geological structures. We selected subsets of the image data of the region of interest acquired by the NaTeCams and stitched them to obtain an overall large field-of-view image of the area (see Table. S1).

The Mars Rover Penetrating Radar (RoPeR) is an ultra-wideband GPR with dual-frequency channels (CH1:15:95 MHz; CH2:0.45-2.15 GHz) designed to investigate the geophysical nature of the subsurface along the rover path[3]. The CH1's antenna is inherited from the Chang'e-3 mission, which was also used to detect relatively deep substructures. The antenna for CH2 (0.45-2.15 GHz) is a Vivaldi type consisting of two perpendicular transmitting and receiving elements. High and low-frequency channels with a vertical resolution of a few centimeters and a few meters can be used alongside. The RoPeR also adopts a linear frequency-modulated signal as its transmitted signal. Further, to avoid the use of high working voltages, it can also provide higher transmission power compared to pulsed signals. Radar data from the high-frequency channel (CH-2) is used in this work to derive the shallow subsurface structure. The IDs of CH2 data are listed in Table S2.

4. Signal Processing of CH2 Data.

The main processing procedures for CH2 data are the following:

Data Reading. The RoPeR data are stored in PDS files. Here we select the data between No. 164 and No. 166 files as an example to show the detailed processing results.

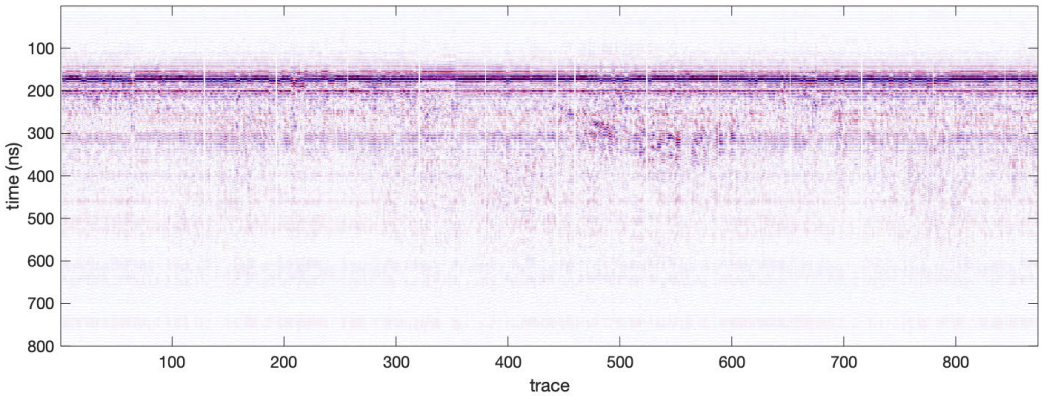

Figure S1. Original data.

Removal of self-detection traces. The receiver conducts a self-detection at every interval during the rover's travel. The self-detection signal is the signal received by the antenna when no signal is transmitted, that is, the background noise that needs to be removed. In the example, most of the self-detection data are separated by 65 data tracks.

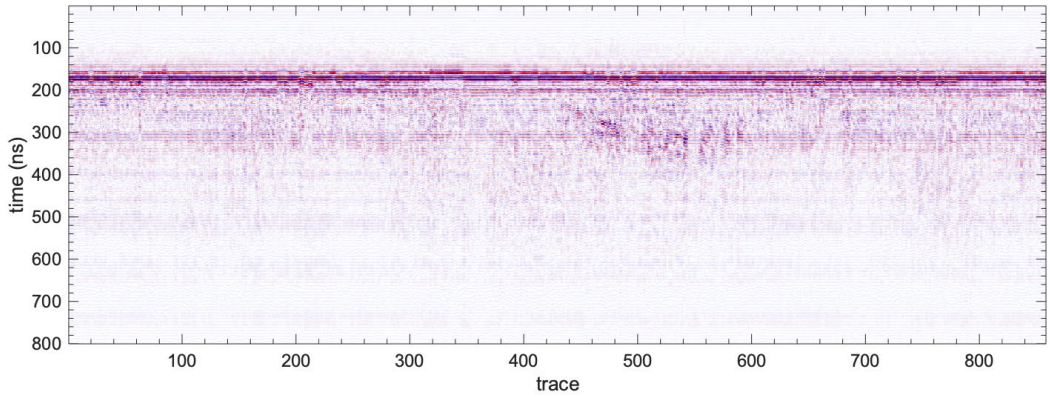

Figure S2. Data after self-detection removal.

Removal of ringing noise. Ringing usually appears as horizontal and periodic events and is a common type of coherent noise in a GPR profile. To eliminate these, we subtracted the horizontal average signal at each A-scan trace.

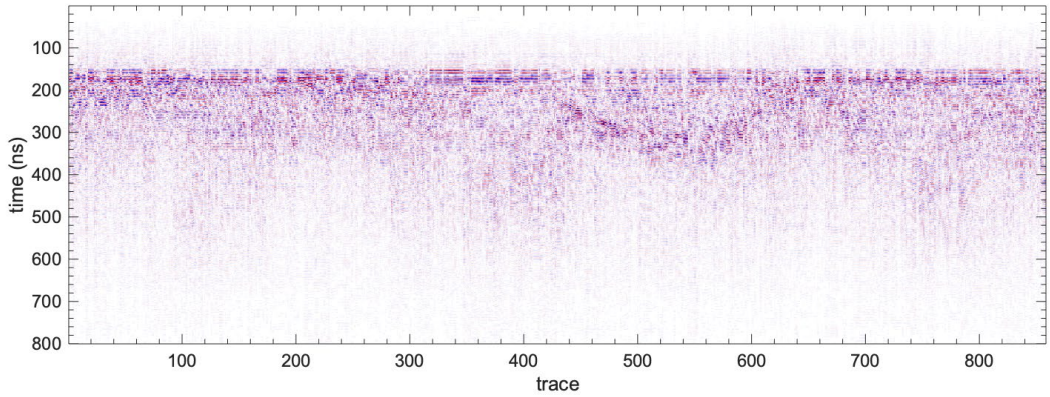

Figure S3. Data after background removal.

Data deduplication. Here we choose the correlation coefficient of two adjacent traces as a criterion for whether the data is duplicated. When the correlation coefficient is greater than 0.95, they are considered to be duplicate data. Their average value will replace these two traces.

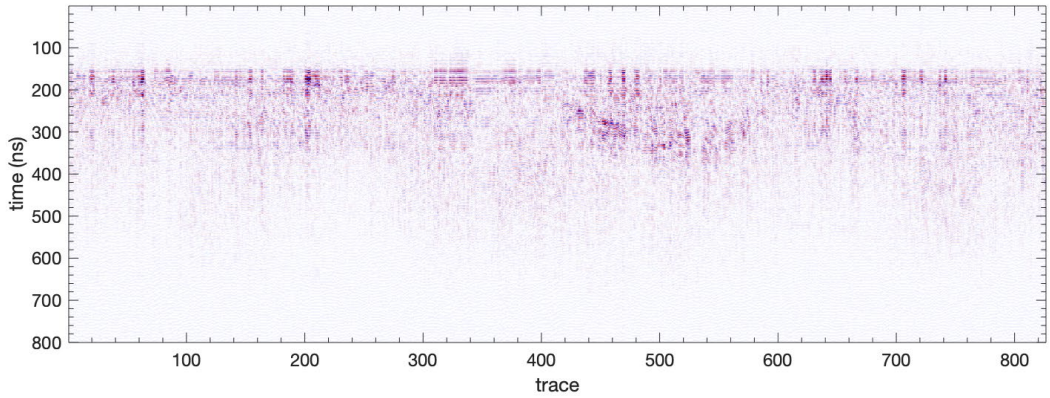

Figure S4. Deduplicated data.

Lateral energy equalization. The energy varies greatly from trace to trace probably due to the interference from the high-frequency antennas. To highlight the weaker signals

swamped with strong signals we use a sliding window to balance the energy intensity in the horizontal direction. Through this processing, signals especially those close to the ground are highlighted.

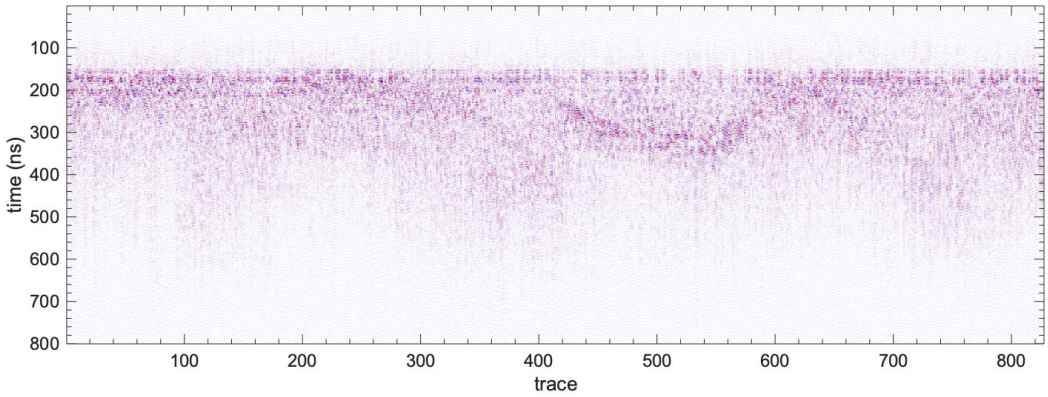

Figure S5. Data after lateral energy equalization.

Gain. The amplitude of electromagnetic waves will attenuate during the propagation in materials, mainly due to dielectric losses and geometric diffusion. As the depth increases, the amplitude of the signals becomes smaller and difficult to analyze. Consequently, they require a boost, which is accomplished by the exponential function compensation method (e.g. Benedetto et al. 2017). It is worth noting that both signals and noise are amplified at the same time.

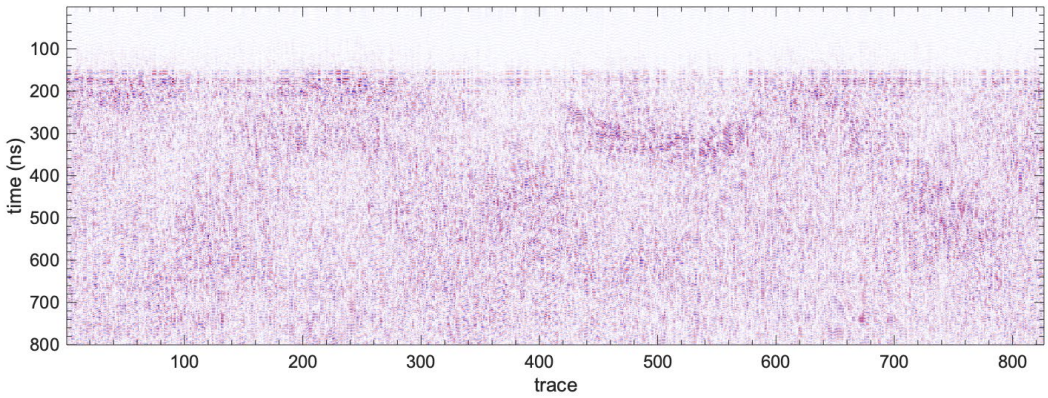

Figure S6. Gain data.

Band-pass filtering. The bandwidth of the transmitted signals of high-frequency data is limited to the range of 0.45 – 2.15 GHz.

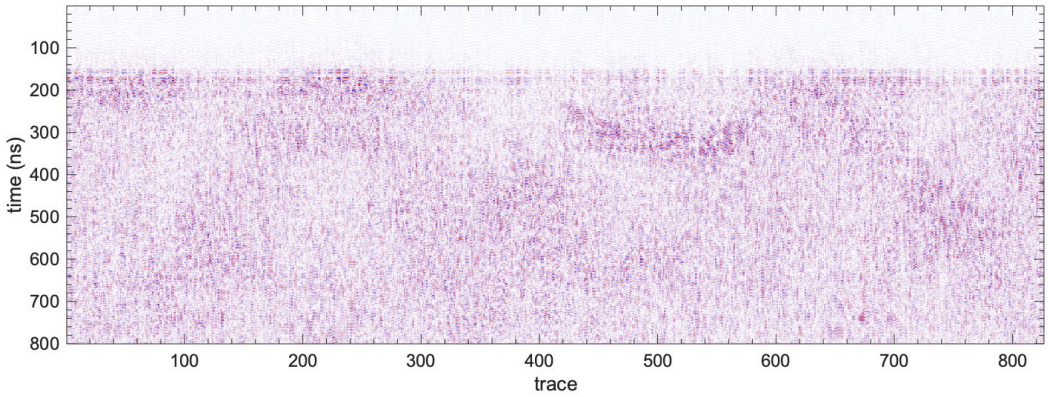

Figure S7. Data after band-pass filtering.

Time-lag adjustment. Invalid data collected during the first ~18 ns are removed.

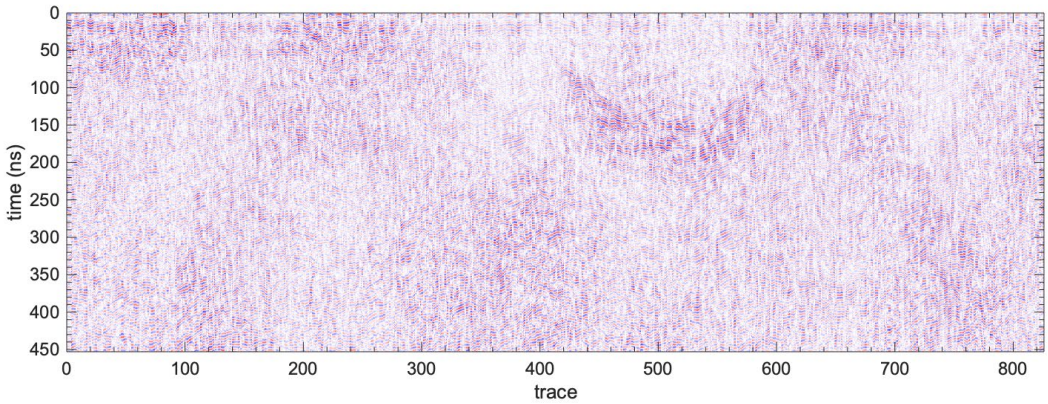

Figure S8. Data after time-lag adjustment.

Kirchhoff migration. We use the amplitudes of the electric field of the received signals to calculate the signals at depth. The dielectric permittivity value chosen here is 3.

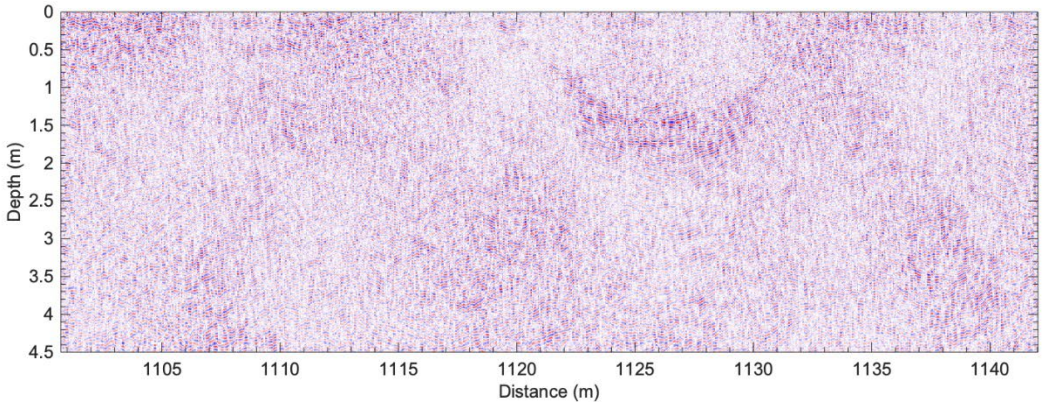

Figure S9. Data after Kirchhoff migration.

5. Loss tangent calculation.

The loss tangent was calculated from the radar range equation and the relationship between loss tangent and attenuation[5], a methodology that has been successfully used in lunar loss

tangent calculations relating to LPR data. The calculation procedure of the loss tangent is as follows (Zhang et al., 2022):

1. We compress the radargram to a single time-dependent function by taking the mean square over all traces at each time.

2. A model-dependent gain function is then applied, and the trace renormalized. Three models of the reflection targets should be considered[5]: for a smooth and planar reflector, $P_r/P_t \propto 1/R^2$; for discrete scatters, $P_r/P_t \propto 1/R^4$; for the Fresnel zone case, $P_r/P_t \propto 1/R^3$.

3. A suitable range would be selected, and then the attenuation η follows simply from the least-squares fit of the two-way distance versus power.

4. According to the relationship between loss tangent and attenuation, the loss tangent is obtained from the attenuation:

$$\tan\delta = \frac{\eta}{9.1\times10^{-8}\sqrt{\varepsilon}f} \quad (9)$$

The result of the loss tangent used in this work is obtained based on the average of all traces.

6. Shallow Subsurface Craters

In Fig. 3C, slightly weaker scattering above the dashed black line may be caused by fine-grained materials mixed with rocks. As depth increases the echoes become weaker below the dashed line. Although the energy drops considerably (after gain), a continuous reflection of the same phase can be seen beneath the section of the crater wall at a depth of ~0.9 m, indicated by a blue dashed line. Some hyperbolic-structure echoes are found between these two lines, possibly caused by debris inside or fractures, which are marked with short, curved black lines.

Another set of echoes with strong reflections at depths of less than 0.4 m was detected at the 93-95 waypoints (Fig. S10). There is a highly degraded crater with a diameter of ~50 meters on the east side of the path, with some visible ejecta stretching close to the path (Fig. S10B). The strong scattering may be caused by ejecta deposits within the continuous ejecta blanket (2.5R or ~ 62.5 m) of this crater.

7. Permittivity selection

We calculate the permittivity from the hyperbola-shaped signal caused by scatter with the geometric model considering the antenna height (Fa et al. 2020). Nearly 100 hyperbolas were extracted to obtain the relative permittivity values of the martian soil in the landing area. Within the effective detection depth of 4.5 m, the average relative permittivity is slightly greater than 3, comparable to the permittivity value of lunar regolith in Chang'e-3 (2.9 ± 0.4, Dong et al. 2017) and Chang'e-4 landing areas (3.6 ± 0.3, Lai et al. 2019) based

on GPR data. For clarity, 3 is selected for time-depth conversion and loss tangent calculation.

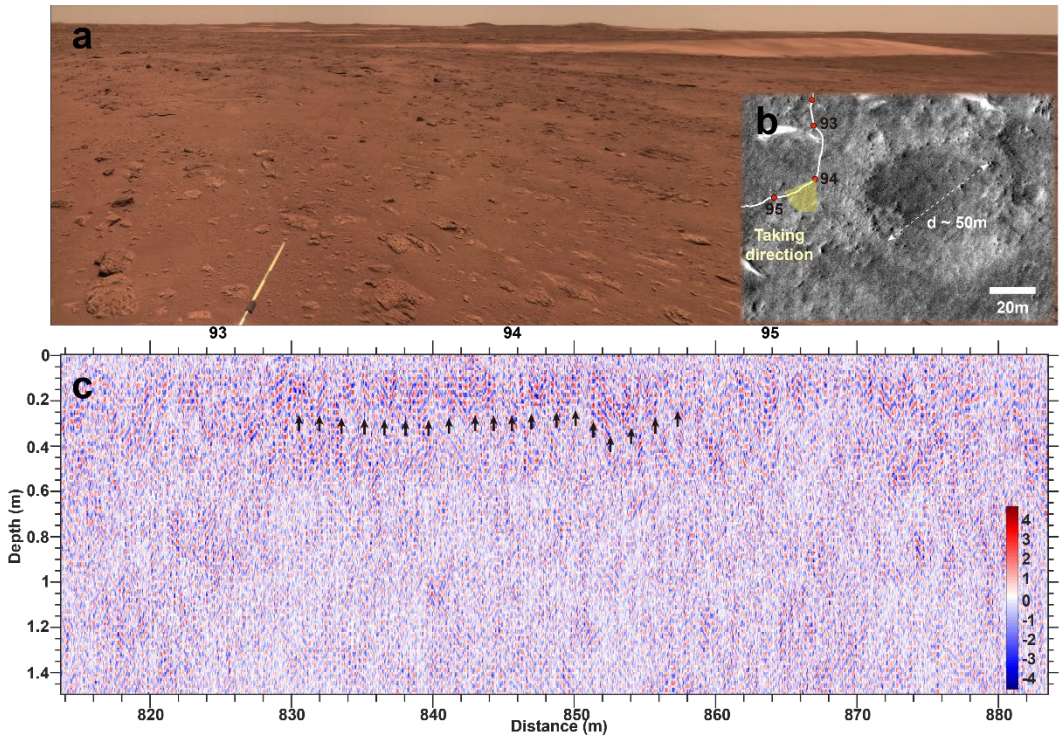

Fig. S10. Terrain image and subsurface radargram of waypoints 93–95.

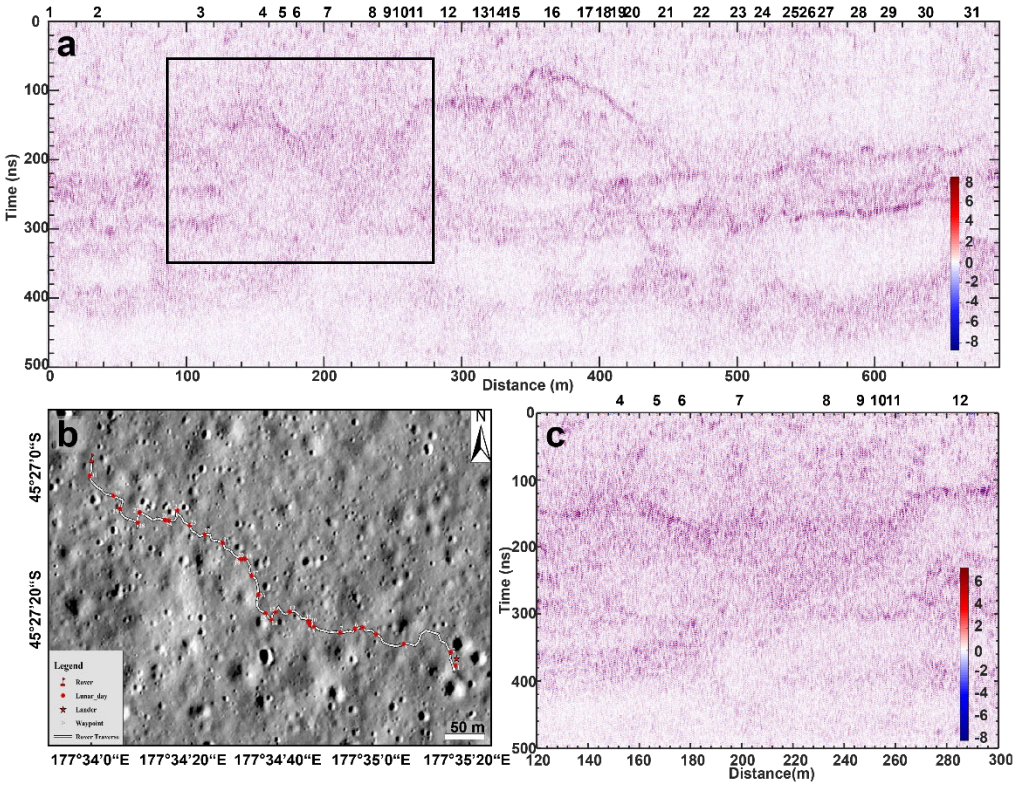

Figure S11. Radargram detected by the LPR of the Chang'e-4 mission. (a) The radargram of the first thirty-one days. (b) Routing path of the Yutu-2 rover. The basemap is a Lunar Reconnaissance Orbiter (LRO) Narrow Angle Camera (NAC) image (File ID: M1314237625LR). (c) The regional radargram of the buried crater is indicated by the black rectangle in (a).

Table S1. The IDs of NaTeCams.

HX1-Ro_GRAS_NaTeCamA-F-001_SCI_N_20210615221152_20210615221152_00032_A.2C
HX1-Ro_GRAS_NaTeCamB-F-011_SCI_N_20210615222759_20210615222759_00032_A.2C
HX1-Ro_GRAS_NaTeCamA-F-012_SCI_N_20210615222917_20210615222917_00032_A.2C
HX1-Ro_GRAS_NaTeCamB-F-002_SCI_N_20210707061358_20210707061358_00053_A.2C
HX1-Ro_GRAS_NaTeCamA-F-003_SCI_N_20210707061516_20210707061516_00053_A.2C
HX1-Ro_GRAS_NaTeCamA-F-002_SCI_N_20210817102509_20210817102509_00093_A.2C
HX1-Ro_GRAS_NaTeCamA-F-003_SCI_N_20210817102644_20210817102644_00093_A.2C
HX1-Ro_GRAS_NaTeCamB-F-004_SCI_N_20210817102836_20210817102836_00093_A.2C
HX1-Ro_GRAS_NaTeCamA-F-004_SCI_N_20210820121205_20210820121205_00096_A.2C
HX1-Ro_GRAS_NaTeCamA-F-003_SCI_N_20210820121030_20210820121030_00096_A.2C
HX1-Ro_GRAS_NaTeCamA-F-002_SCI_N_20210820120855_20210820120855_00096_A.2C
HX1-Ro_GRAS_NaTeCamB-F-002_SCI_N_20210820120912_20210820120912_00096_A.2C
HX1-Ro_GRAS_NaTeCamB-F-003_SCI_N_20210820121047_20210820121047_00096_A.2C
HX1-Ro_GRAS_NaTeCamB-F-004_SCI_N_20210820121222_20210820121222_00096_A.2C
HX1-Ro_GRAS_NaTeCamA-F-005_SCI_N_20210820121340_20210820121340_00096_A.2C
HX1-Ro_GRAS_NaTeCamB-F-005_SCI_N_20210820121357_20210820121357_00096_A.2C
HX1-Ro_GRAS_NaTeCamA-F-004_SCI_N_20211027054530_20211027054530_00162_A.2C
HX1-Ro_GRAS_NaTeCamA-F-005_SCI_N_20211027054705_20211027054705_00162_A.2C
HX1-Ro_GRAS_NaTeCamA-F-006_SCI_N_20211027054840_20211027054840_00162_A.2C

Table S2. The IDs of CH2 data of RoPeR.

HX1-Ro_GRAS_RoPeR-HF-HH_SCI_N_20210525042001_20210525043243_00011_A.2C
HX1-Ro_GRAS_RoPeR-HF-HH_SCI_N_20210528062805_20210528063800_00014_A.2C
HX1-Ro_GRAS_RoPeR-HF-HH_SCI_N_20210530073623_20210530074230_00016_A.2C
HX1-Ro_GRAS_RoPeR-HF-HH_SCI_N_20210605100445_20210605101554_00022_A.2C
HX1-Ro_GRAS_RoPeR-HF-HH_SCI_N_20210606104402_20210606105856_00023_A.2C
HX1-Ro_GRAS_RoPeR-HF-HH_SCI_N_20210607112519_20210607114327_00024_A.2C
HX1-Ro_GRAS_RoPeR-HF-HH_SCI_N_20210608120247_20210608122320_00025_A.2C
HX1-Ro_GRAS_RoPeR-HF-HH_SCI_N_20210609124205_20210609130229_00026_A.2C
HX1-Ro_GRAS_RoPeR-HF-HH_SCI_N_20210610132123_20210610133816_00027_A.2C
HX1-Ro_GRAS_RoPeR-HF-HH_SCI_N_20210611140040_20210611142216_00028_A.2C
HX1-Ro_GRAS_RoPeR-HF-HH_SCI_N_20210612143959_20210612150247_00029_A.2C
HX1-Ro_GRAS_RoPeR-HF-HH_SCI_N_20210613151917_20210613154608_00030_A.2C
HX1-Ro_GRAS_RoPeR-HF-HH_SCI_N_20210614155835_20210614162453_00031_A.2C
HX1-Ro_GRAS_RoPeR-HF-HH_SCI_N_20210616171702_20210616172557_00033_A.2C
HX1-Ro_GRAS_RoPeR-HF-HH_SCI_N_20210617172542_20210617174251_00034_A.2C
HX1-Ro_GRAS_RoPeR-HF-HH_SCI_N_20210618180500_20210618183135_00035_A.2C
HX1-Ro_GRAS_RoPeR-HF-HH_SCI_N_20210619184419_20210619190603_00036_A.2C
HX1-Ro_GRAS_RoPeR-HF-HH_SCI_N_20210623212136_20210623214627_00040_A.2C
HX1-Ro_GRAS_RoPeR-HF-HH_SCI_N_20210625224006_20210625224957_00042_A.2C
HX1-Ro_GRAS_RoPeR-HF-HH_SCI_N_20210627235846_20210628000439_00044_A.2C
HX1-Ro_GRAS_RoPeR-HF-HH_SCI_N_20210630005145_20210630005917_00046_A.2C
HX1-Ro_GRAS_RoPeR-HF-HH_SCI_N_20210702023607_20210702024818_00048_A.2C
HX1-Ro_GRAS_RoPeR-HF-HH_SCI_N_20210703024448_20210703031223_00049_A.2C
HX1-Ro_GRAS_RoPeR-HF-HH_SCI_N_20210705040330_20210705043031_00051_A.2C
HX1-Ro_GRAS_RoPeR-HF-HH_SCI_N_20210706044251_20210706050950_00052_A.2C
HX1-Ro_GRAS_RoPeR-HF-HH_SCI_N_20210707052212_20210707054915_00053_A.2C
HX1-Ro_GRAS_RoPeR-HF-HH_SCI_N_20210708060134_20210708062910_00054_A.2C
HX1-Ro_GRAS_RoPeR-HF-HH_SCI_N_20210709064055_20210709070830_00055_A.2C
HX1-Ro_GRAS_RoPeR-HF-HH_SCI_N_20210710064927_20210710071803_00056_A.2C
HX1-Ro_GRAS_RoPeR-HF-HH_SCI_N_20210711072849_20210711075606_00057_A.2C
HX1-Ro_GRAS_RoPeR-HF-HH_SCI_N_20210713084733_20210713091534_00059_A.2C
HX1-Ro_GRAS_RoPeR-HF-HH_SCI_N_20210714092655_20210714095429_00060_A.2C
HX1-Ro_GRAS_RoPeR-HF-HH_SCI_N_20210715100617_20210715103221_00061_A.2C
HX1-Ro_GRAS_RoPeR-HF-HH_SCI_N_20210716104539_20210716111239_00062_A.2C
HX1-Ro_GRAS_RoPeR-HF-HH_SCI_N_20210717113015_20210717115246_00063_A.2C
HX1-Ro_GRAS_RoPeR-HF-HH_SCI_N_20210718120424_20210718122235_00064_A.2C
HX1-Ro_GRAS_RoPeR-HF-HH_SCI_N_20210720132309_20210720135038_00066_A.2C
HX1-Ro_GRAS_RoPeR-HF-HH_SCI_N_20210721140232_20210721142946_00067_A.2C
HX1-Ro_GRAS_RoPeR-HF-HH_SCI_N_20210722144155_20210722151614_00068_A.2C
HX1-Ro_GRAS_RoPeR-HF-HH_SCI_N_20210724160042_20210724162803_00070_A.2C
HX1-Ro_GRAS_RoPeR-HF-HH_SCI_N_20210725164005_20210725170755_00071_A.2C
HX1-Ro_GRAS_RoPeR-HF-HH_SCI_N_20210726171928_20210726174721_00072_A.2C
HX1-Ro_GRAS_RoPeR-HF-HH_SCI_N_20210727175852_20210727182248_00073_A.2C
HX1-Ro_GRAS_RoPeR-HF-HH_SCI_N_20210728180726_20210728183822_00074_A.2C
HX1-Ro_GRAS_RoPeR-HF-HH_SCI_N_20210729184650_20210729191424_00075_A.2C
HX1-Ro_GRAS_RoPeR-HF-HH_SCI_N_20210730192614_20210730195423_00076_A.2C

HX1-Ro_GRAS_RoPeR-HF-HH_SCI_N_20210801204502_20210801211253_00078_A.2C
HX1-Ro_GRAS_RoPeR-HF-HH_SCI_N_20210803220350_20210803223708_00080_A.2C
HX1-Ro_GRAS_RoPeR-HF-HH_SCI_N_20210804224315_20210804231025_00081_A.2C
HX1-Ro_GRAS_RoPeR-HF-HH_SCI_N_20210805232239_20210805234944_00082_A.2C
HX1-Ro_GRAS_RoPeR-HF-HH_SCI_N_20210807000204_20210807001938_00083_A.2C
HX1-Ro_GRAS_RoPeR-HF-HH_SCI_N_20210812031908_20210812034809_00088_A.2C
HX1-Ro_GRAS_RoPeR-HF-HH_SCI_N_20210813035833_20210813042708_00089_A.2C
HX1-Ro_GRAS_RoPeR-HF-HH_SCI_N_20210814043758_20210814050320_00090_A.2C
HX1-Ro_GRAS_RoPeR-HF-HH_SCI_N_20210815051714_20210815052713_00091_A.2C
HX1-Ro_GRAS_RoPeR-HF-HH_SCI_N_20210817092230_20210817095422_00093_A.2C
HX1-Ro_GRAS_RoPeR-HF-HH_SCI_N_20210818095652_20210818102427_00094_A.2C
HX1-Ro_GRAS_RoPeR-HF-HH_SCI_N_20210819103127_20210819105944_00095_A.2C
HX1-Ro_GRAS_RoPeR-HF-HH_SCI_N_20210820110626_20210820113519_00096_A.2C
HX1-Ro_GRAS_RoPeR-HF-HH_SCI_N_20210821114147_20210821122327_00097_A.2C
HX1-Ro_GRAS_RoPeR-HF-HH_SCI_N_20210822121730_20210822122701_00098_A.2C
HX1-Ro_GRAS_RoPeR-HF-HH_SCI_N_20210825140654_20210825143235_00101_A.2C
HX1-Ro_GRAS_RoPeR-HF-HH_SCI_N_20210826144406_20210826151304_00102_A.2C
HX1-Ro_GRAS_RoPeR-HF-HH_SCI_N_20210828155937_20210828162807_00104_A.2C
HX1-Ro_GRAS_RoPeR-HF-HH_SCI_N_20210829163755_20210829164544_00105_A.2C
HX1-Ro_GRAS_RoPeR-HF-HH_SCI_N_20210830171634_20210830174323_00106_A.2C
HX1-Ro_GRAS_RoPeR-HF-HH_SCI_N_20210831175535_20210831182145_00107_A.2C
HX1-Ro_GRAS_RoPeR-HF-HH_SCI_N_20210901183456_20210901190107_00108_A.2C
HX1-Ro_GRAS_RoPeR-HF-HH_SCI_N_20210902191440_20210902193841_00109_A.2C
HX1-Ro_GRAS_RoPeR-HF-HH_SCI_N_20210904203509_20210904211803_00111_A.2C
HX1-Ro_GRAS_RoPeR-HF-HH_SCI_N_20210905211555_20210905212520_00112_A.2C
HX1-Ro_GRAS_RoPeR-HF-HH_SCI_N_20210906215702_20210906220332_00113_A.2C
HX1-Ro_GRAS_RoPeR-HF-HH_SCI_N_20211029052245_20211029055203_00164_A.2C
HX1-Ro_GRAS_RoPeR-HF-HH_SCI_N_20211031070239_20211031073127_00166_A.2C
HX1-Ro_GRAS_RoPeR-HF-HH_SCI_N_20211103093104_20211103094940_00169_A.2C
HX1-Ro_GRAS_RoPeR-HF-HH_SCI_N_20211106113023_20211106115325_00172_A.2C
HX1-Ro_GRAS_RoPeR-HF-HH_SCI_N_20211115172822_20211115175629_00181_A.2C
HX1-Ro_GRAS_RoPeR-HF-HH_SCI_N_20211125235732_20211126002616_00191_A.2C

Supplementary Reference:

Bandfield, J. L., Giotch, T. D., and Christensen, P. R. 2003. Spectroscopic identification of carbonate minerals in the Martian dust. Science 301 p. 1084-1087.

Benedetto, A., Tosti, F., Ciampoli, L. B., & D'amico, F. (2017). An overview of ground-penetrating radar signal processing techniques for road inspections. Signal processing, 132, 201-209.

Berger, J. A., Schmidt, M. E., Gellert R., Campbell, J. L., King, P. L., Flemming, R. L., Ming, D. W., Clark, B. C., Pradier, I., Vanbommel, S. J. Y., Minitti, M. E., Fairén, A. G., Boyd, N. I., Thompson, L. M., Perrett, G. M., Ellioll, B. E., and Desouza, E. 2016. A global Mars dust composition refined by the Alpha-Particle X-ray Spectrometer in Gale Crater, 43 p. 67-75.

Blake, D. F., Morris, R. Y., Kocurek, G., Morrison, S. M., Downs, R. T., Bish, D., Ming, D. W., Edgell, K. S., Rubin, D., Goetz, W., Madsen, M. B., Sullivan, R., Gellert, R., Campbell, I., Treiman, A. H., Mclennan, S. M., Yen, A. S., Grotzinger, J., Vaniman, D. T., Chipera, S. J., Achilles, C. N., Rampe, E. B., Sumner, D., Meslin, P. Y., Maurice, S., Forni, O., Gasnault, 0., Fisk, M., Schmidt, M., Mahaffy, P., Leshin, L. A., Glavin, D., Steele, A., Freissinet, C., and, Navarro-González, R. 2013. MSL Science Team, 341 p. 1239505-1239505.

Christensen, P. R. 2008. Global Mineralogy Mapped from the Mars Global Surveyor Thermal Emission Spectrometer In The Martian Surface: Composition, Mineralogy, and Physical Properties, pages 197-197. Cambridge University Press.

Dong, Z., Fang, G., Ji, Y., Gao, Y., Wu, C., and Zhang, X. 2017. Parameters and structure of lunar regolith in Chang'E-3 landing area from lunar penetrating radar (LPR) data, Icarus, 282 p. 40-46.

Fa, W., 2020. Bulk Density of the Lunar Regolith at the Chang'E-3 Landing Site as Estimated From Lunar Penetrating Radar. Earth Planet. Phys. 7, e2019EA000801.

Goetz, W., Bertelsen, P., Binau, C. S., Gunnlaugsson, H. P., Hviid, S. F., Kinch, K. M., Madsen, D. E., Madsen, M. B., Olsen, M., Gellert, R., Klingelhöfer, G., Ming, D. W., Monis, R. V., Rieder, R., Rodionov, D. S., Souza P. A. D., Schröder, C., Squyres, S. W., Wdowiak, T., and Yen, A. 2005. Indication of drier periods on Mars from the chemistry and mineralogy of atmospheric dust. Nature, 436 p. 62-65.

Kirk, R. L., Howington -Kraus, E., Rosiek, M. R., Anderson, J. A., Archinal, B. A., Becker, K. J., Cook, D. A., Galuszka, D. M., -Geissler, P. E., Hare, T. M., Holmberg, I. M., Keszthelyi, L. P., Redding, B. L., Delamere, W. A., Gallagher, D., Chapel, J. D., Eliason, E. M., King, R., and McEwen, A. S. 2008. Ultrahigh resolution topographic mapping of Mars with MRO HiRISE stereo images: Meter-scale slopes of candidate Phoenix landing sites. J. Geophys. Res.

113 p. 0-24.

Lai J., Xu, Y., Zhang, X., Xiao, L., Yan, Q., Meng, X., Zhou, B., Dong, Z., Zhao, D. 2019. Comparison of dielectric properties and structure of lunar regolith at Chang'e-3 and Chang'e-4 landing sites revealed by ground-penetrating radar. Geophys. Res. Lett. 46 p. 12783–12793.

Mcsween, H. Y., McGlynn, I. O., and Rogers, A. D. 2010. Determining the modal mineralogy of Martian soils, J. Geophys. Res. 115. P.0-12.

McEwen, A. S., Eliason, E. M., Bergstrom, J. W., Bridges, N. T., Hansen, C. J., Delamere, W., Grant, J. A., Gulick, V. C., Herkenhoff, K. E. , Keszthelyi, L., Kirk, R. L., Mellon, M. T., Squyres, S. W. , Thomas, N., Weitz, C. M. (2007). Mars Reconnaissance Orbiter's High Resolution Imaging Science Experiment (HiRISE), J. Geophys. Res., 112, E05S02, doi:10.1029/2005JE002605.

Rogers, A. D. and Aharonson, O. 2008. Mineralogical composition of sands in Meridiani Planum determined from Mars Exploration Rover data and comparison to orbital measurements. J. Geophys. Res, 113 p. 6-14.

Ruff, S. W. and Christensen, P. R. 2002. Bright and dark regions on Mars: Particle size and mineralogical characteristics based on Thermal Emission Spectrometer data. J. Geophys. Res., 107 p. 5127-5127.

Ruff, S. W., Christensen, P.R., Blaney, D. L., Farrand, W. H., Johnson, J. R., Michalski, J.E., Moersch, J. E., Wright, S. P., and Squyres, S. W. 2006. The rocks of Gusev Crater as viewed by the Mini-TES instrument. J. Geophys. Res, 111. P. 12-18.

Zhang, L., Xu, Y., Chen, R., Wong, H. K., Lai, J., Meng, X., and Chen, R., Zeng, Z., Feng, X., and Liu, C. 2022. Calculation of dielectric constant, loss property and scattering characteristics from the future martian GPR data. Icarus, 386. 115181.